Computational Materials Science 239 (2024) 112962

Contents lists available at ScienceDirect

Computational Materials Science

journal homepage: www.elsevier.com/locate/commatsci

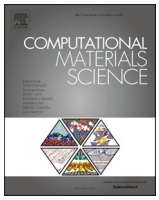

Full Length Article

Theoretical exploration of ternary nitrides for high-efficiency ferroelectric photovoltaics

Guo-Xia Lai [a], Jin-Long Yang [a], Hua-Kai Xu [a], Wen-Ce Li [a], Kun-Ren Su [a], Xiang-Fu Xu [a], Wei-Ling Zhu [a], Xing-Yuan Chen [a,*], Xiao-Bao Yang [b], Yu-Jun Zhao [b]

[a] Department of Physics, School of Science, Guangdong University of Petrochemical Technology, Maoming, Guangdong 525000, PR China
[b] Department of Physics, South China University of Technology, Guangzhou 510640, PR China

ARTICLE INFO

Keywords:
Ternary nitride
Ferroelectric
Photovoltaics
High efficiency
First-principles calculation

ABSTRACT

Although nitride materials hold great functional promise, ferroelectric photovoltaic nitrides remain relatively rare within the scientific community. In this study, high-throughput calculations have been employed to explore and predict novel stable ternary nitrides characterized by both high photoelectric conversion efficiency and robust ferroelectric polarization. Notable candidates, including Mg_2CrN_3, Mg_2MnN_3, $MgVN_2$, $ZnVN_2$, and X_2BiN_3 (where X represents Mg, Ca, and Sr), are anticipated to exhibit remarkable ferroelectric photovoltaic properties, with a particular emphasis on efficiently harnessing visible light. The incorporation of early 3d transition metals and bismuth (Bi) elements within ternary metal nitrides is highlighted as a key strategy for achieving high ferroelectric photovoltaic efficiency. Furthermore, these ferroelectric nitrides demonstrate relatively high carrier mobilities, which are conducive to facilitating the transport of photogenerated carriers driven by ferroelectricity. This research offers a selection of promising ternary nitride candidates with substantial potential for application in the field of ferroelectric photovoltaics.

1. Introduction

Ferroelectric materials have aroused interest in photovoltaics since they have the internal electric field to rapidly separate photogenerated carriers without p-n junctions [1]. Ferroelectric oxides have been popular and widely studied in ferroelectric photovoltaics property of their excellent stability and high ferroelectric polarization [2–4]. $BiFeO_3$ has an anomalous photovoltaic effect with ultra-high open-circuit voltage [5]. However, most ferroelectric oxides have more significant band gaps and harvest visible light poorly [6]. Organic-inorganic halide perovskite materials represented by $MAPbI_3$ have attracted much attention in the photovoltaic field due to their ultra-high photoelectric conversion efficiency, but there is still some controversy about their ferroelectric behavior or weak ferroelectric polarization strength [7,8]. The ambiguity of the ferroelectric mechanism, environmental unfriendliness, and low polarization of halides are unfavorable for the ferroelectric photovoltaics application.

The difficulty of synthesizing nitrides has limited researches on nitrides much less than on those widely studied oxides and halides [9]. However, more and more new ternary metal nitrides have been theoretically proposed and experimentally prepared with the development of large-scale computing conditions and advanced experimental methods [10–12]. Sarmiento-Pérez et al predicted nitride perovskite materials by the thermodynamic stability [13]. Zakutayev reviewed the design progress of novel semiconductor nitrides in solar energy conversion technology, considering that nitrides have better solar energy absorption and electrical transport properties than widely studied oxides [14]. Through large-scale calculations, Sun et al established a large-scale inorganic ternary metal nitride stability phase diagram and uploaded the structure to the Materials Project [15]. $CaZn_2N_2$ was predicted to be a stable ternary nitride semiconductor and had been successfully prepared by a high-pressure method [16]. Heinselman et al prepared Mg_3SbN and Mg_2SbN_3 ternary nitride films by sputtering deposition and proposed that Mg_3SbN films have excellent prospects in photovoltaics [17]. $LaWN_3$[18], $LaMoN_3$ [19], and Mg_2XN_3 (X = V, Cr) [20] are theoretically predicted as potential stable ferroelectric nitrides. $LaWN_3$ film is the first stable polar perovskite structure with potential ferroelectric behavior experimentally [21]. $CeNbN_3$ and $CeTaN_3$ nitrides have been proposed as a new class of nitride semiconductors with strong visible light absorption [22]. Zn_2VN_3 is a weakly doped p-type

* Corresponding author.
E-mail address: chenxingyuan@gdupt.edu.cn (X.-Y. Chen).

https://doi.org/10.1016/j.commatsci.2024.112962
Received 14 December 2023; Received in revised form 12 March 2024; Accepted 18 March 2024
Available online 23 March 2024

semiconductor that exhibits room-temperature photoluminescence across the band gap range of 2 to 3 eV [23]. Xue et al found $MgTiN_2$ and $ZnSnN_2$ are suggested to be promising photovoltaic materials for their high photoelectric conversion efficiency and small carrier effective mass through high-throughput calculations [24]. We have recently found that Mg_2XN_3 (X = Sb, Ta, Bi and Nb) have the excellent ferroelectric property for energy conversion applications in photovoltaic cells and photocatalytic hydrogen production through first principles calculations [25]. Although much progress has been achieved in exploring ferroelectricity and semiconductor properties of ternary metal nitrides, the development and investigation of ferroelectric photovoltaic properties are still relatively scarce compared to those of oxides and halides. The Materials Genome Project has provided a new way for the development of materials in a faster and more cost-effective process [26,27].

Here we have conducted high-throughput calculations to search for ternary nitrides as ferroelectric photovoltaics materials based on the materials gene library site (Materials Project). Mg_2CrN_3, Mg_2MnN_3, $MgVN_2$, $ZnVN_2$ and X_2BiN_3 (X = Mg, Ca, and Sr) have been suggested to be highly efficient ferroelectric photovoltaic candidates prevailing the much studied ferroelectric oxides or sulfides. The ternary metal nitrides with early 3*d* transition metals or Bi elements could have high spontaneous ferroelectric strength and photoelectric conversion efficiency.

2. Initial selection of ferroelectric photovoltaic ternary nitrides

The ternary nitrides with lower convex hull energy, polar space groups and suitable band gaps have been selected by the pymatgen program [28] from the Materials Project. Crystals with ten polar point groups could have spontaneous ferroelectric polarization due to symmetry breaking. 1(C1), 2(C2), 3(C3), 4(C4), 6(C6), m(Cs), mm2(C2v), 4 mm(C4v), 3 m(C3v), 6 mm(C6v) etc point groups have been used to detect the potential ferroelectric materials. After the ternary nitrides are selected by the polar space groups, the potential stable structures are further selected by the condition of low convex hull energy (less than 0.01 eV) and the number of atoms less than 40. The number of atoms is kept within 40 in consideration of the computational cost. The band gap values of the material should be controlled between 1 and 3 eV for massive visible light harvesting. The band gap is set to be greater than 1 eV since the leakage current will dominate to suppress ferroelectric polarization if the band gap is too small. The condition for the band gap to be less than 3 eV is to ensure that the material absorbs visible light. Considering that part of the band gap calculation in the Materials Project is based on the Perdew-Burke-Ernzerhof (PBE) functional, the PBE functional generally underestimates the band gap values [29,30]. We set the band gap screening standard to 0–3 eV as much as possible without leaving out potential structures since some of the band gap values could be underestimated in the Materials Project. The potential stable ferroelectric photovoltaic ternary nitrides can be initially selected from the Materials Project based on these convex hull energy, space group, and band gap values criteria. As a result, 77 tenary nitrides meet the criteria out of the 4848 tenary nitrides in the Materials Project (June 2022). The band gaps of these selected 77 ternary nitrides are further calculated by the more accurate HSE06 functional (see Table 1). The band gaps calculated by HSE06 functional are usually in line with the available experimental values [31,32]. Consequently, 27 out of 77 structures are confirmed to possess of band gaps ranging from 1 ~ 3 eV, displayed in

Table 1
The band gap values and polar space group of ternary nitrides.

Compounds	Space Group	Present HSE06(eV)	Materials Project (eV)	Compounds	Space Group	Present HSE06 (eV)	Materials Project (eV)
$Ag_2N_2O_6$	R3c	3.62	1.86	$Mn_1Co_1N_2$	R3m	0.00	0.00
$Ag_7N_1O_{11}$	Fmm2	0.00	0.00	$Mn_2Zn_4N_6$	$Cmc2_1$	0.68	0.00
$Al_1Ga_1N_2$	P3m1	3.87	2.72	$Mo_2C_1N_1$	Pmm2	0.00	0.00
$Al_1Ga_3N_4$	Pm	3.30	2.24	$Na_{12}Mo_4N_{12}$	Cc	2.35	1.43
$Ba_4Si_{10}N_{16}$	$Pmn2_1$	4.06	2.89	$Na_{12}Mo_8N_{20}$	$I4_1$	2.38	1.93
$Ca_{10}Nb_2N_{10}$	Cm	1.52	0.72	$Na_{12}W_4N_{12}$	Cc	2.77	1.77
$Ca_1H_1N_1$	I4mm	3.32	2.44	$Na_{12}W_8N_{20}$	$I4_1$	2.88	2.32
$Ca_3U_1N_4$	Fmm_2	–	1.42	$Na_1N_1O_2$	Imm2	4.42	2.48
$Ca_4Sn_4N_8$	$Pna2_1$	2.26	1.38	$Na_2Fe_2N_2$	$P6_3mc$	1.18	0.50
$Cd_4Ge_4N_8$	$Pna2_1$	1.83	0.95	$Na_2Ge_4N_6$	$Cmc2_1$	3.56	2.34
$Ce_6Si_{12}N_{22}$	P4bm	–	−0.32	$Na_8N_8O_{24}$	P1	4.57	2.57
$Cs_{12}Re_8N_{20}$	$I4_1$	0.60	0.32	$Na_8Re_2N_6$	Cc	3.64	2.45
$Ga_1N_5O_{14}$	C2	3.28	1.26	$Nb_2Zn_4N_6$	$Cmc2_1$	3.02	1.93
$Ge_4N_4O_2$	$Cmc2_1$	3.93	2.64	$P_4N_3Cl_{11}$	R3	3.87	2.66
$Hf_{16}N_{16}O_8$	P1	3.22	1.99	$Pb_4C_4N_8$	$Pna2_1$	2.52	1.86
$Hf_1Zn_1N_2$	P3m1	3.51	2.28	$Rb_{12}W_8N_{20}$	$I4_1$	3.02	2.05
$Hg_8N_8O_{24}$	$P2_1$	4.16	2.59	$S_6N_4O_{28}$	Cc	3.40	1.42
$Ir_1N_4C_{l6}$	I4mm	0.00	0.31	$Sr_{12}Cu_6N_{10}$	$P4_2mc$	1.53	0.49
$K_{12}W_8N_{20}$	$I4_1$	3.15	2.18	$Sr_2W_2N_6$	P1	1.98	1.08
$K_1N_1O_2$	Cm	4.40	2.50	$Ta_2Zn_4N_6$	$Cmc2_1$	3.49	2.36
$K_2Ge_4N_6$	$Cmc2_1$	2.70	1.57	$Ta_9N_3O_{18}$	Cm	3.58	2.16
$K_6N_2O_6$	I4cm	1.23	0.22	$Ti_4Zn_4N_8$	$Pna2_1$	3.56	2.37
$La_2W_2N_6$	R3c	2.09	1.29	$Ti_6N_4O_6$	Cm	2.84	1.55
$Li_{14}I_2N_4$	Cm	2.77	1.67	$V_2Zn_4N_6$	$Cmc2_1$	2.41	1.33
$Li_{16}H_8N_8$	Ima2	3.86	2.56	$Zn_2Mo_2N_4$	P6_3mc	0.56	0.00
$Li_{16}Se_2N_4$	$I4_1md$	2.84	2.04	$Zn_3Sb_1N_3$	$Cmc2_1$	2.61	0.00
$Li_{16}Te_2N_4$	$I4_1md$	3.44	2.52	$Zn_4Cr_2N_6$	$Pna2_1$	0.77	0.00
$Li_1Mo_1N_2$	R3m	0.00	0.00	$Zn_4Cr_4N_8$	$Pna2_1$	0.36	1.70
$Li_2Ge_4N_6$	$Cmc2_1$	3.90	2.58	$Zn_4Ge_4N_8$	$Cmc2_1$	2.84	2.60
$Li_4V_4N_8$	$Pna2_1$	2.30	1.31	$Zn_4P_2N_6$	$Cmc2_1$	3.95	0.00
$Mg_4Cr_2N_6$	$Cmc2_1$	1.52	0.00	$Zn_4Re_2N_6$	$Cmc2_1$	0.31	0.19
$Mg_4Cr_4N_8$	$Pna2_1$	0.39	0.00	$Zn_4Sb_2N_6$	$Pna2_1$	1.14	0.12
$Mg_4Ge_4N_8$	$Pna2_1$	3.78	2.64	$Zn_4Sn_4N_8$	$Pmn2_1$	1.05	2.11
$Mg_4Sb_2N_6$	$Cmc2_1$	2.34	1.36	$Zn_6Mo_2N_8$	Cm	3.21	1.38
$Mg_4Sn_4N_8$	$Pna2_1$	2.02	1.06	$Zn_6W_2N_8$	$Pmn2_1$	3.66	2.46
$Mg_4Ta_2N_6$	$Cmc2_1$	4.22	2.94	$Zn_8N_4Cl_4$	$Pna2_1$	3.20	1.97
$Mg_4V_2N_6$	$Cmc2_1$	3.05	1.84	$Zr_{16}N_{16}O_8$	P1	2.76	1.65
$Mg_6Mo_2N_8$	$Pmn2_1$	4.14	2.98	$Zr_1Zn_1N_2$	P3m1	3.13	2.00
				$Zr_6N_4O_6$	Cm	3.84	2.55

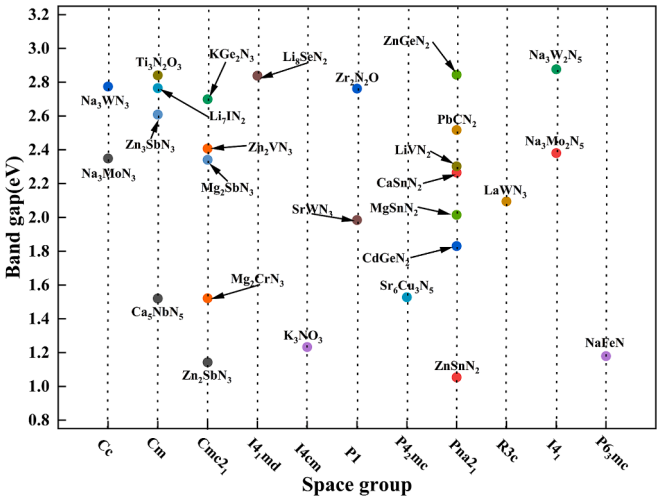

Fig. 1. The ternary nitrides with polar structure in the band gap range of 1–3 eV.

Fig. 1. All the ternary nitrides in Fig. 1 are potential ferroelectric photovoltaic materials, satisfying the polar space group and band gap conditions.

3. Prediction of promising ferroelectric photovoltaic ternary nitrides

The polar space group structure with higher frequency is selected from Fig. 1 as the predicted parents, and the offspring is generated by the element replacement method. Progeny is produced by randomly combining pairs of elements of the same family and chemical valence in the periodic table of elements. Inspired by genetic eugenics, the $Cmc2_1$ structure (X_2YN_3) and the $Pna2_1$ structure (XYN_2) appear most frequently in Fig. 1, and their respective components have a higher probability of producing highly efficient ferroelectric photovoltaic ternary nitrides. Based on conditions such as element valence matching and environmental friendliness, the predicted possible combinations of ternary nitrides are arranged, as shown in Fig. 2. The random combination generated $Cmc2_1$ structures (X_2YN_3) and $Pna2_1$ structures (XYN_2) after excluding the repeated structures in the Materials Project, leaving 44 and 51 structures, respectively. The calculation of the band gap of HSE06 is carried out for 95 structures, and the calculated structures are shown in the Supporting Information (SI) (see Table S1). There are fifteen $Cmc2_1$ structures (X_2YN_3) and ten $Pna2_1$ structures (XYN_2) that meet the band gap requirements. Their phonon dispersion relations were calculated to verify the structural stability of these 25 predicted materials. The calculation phonon dispersion results are shown in Supporting Information (SI) (see Figure S1). The materials that satisfy the stability condition without imaginary frequency are Ca_2BiN_3, Ca_2SbN_3, Mg_2BiN_3, Mg_2MnN_3, Sr_2BiN_3, $BaHfN_2$, $BaSnN_2$, $MgHfN_2$, $MgTiN_2$, $MgZrN_2$, $MgVN_2$, $SrSnN_2$, $ZnVN_2$ respectively.

Crystals of $MgHfN_2$, $MgTiN_2$ and $MgZrN_2$ are close to the centrosymmetric structure, which could be absence of ferroelectricity. The elastic coefficients of the predicted ternary nitrides were calculated to further verify the kinetic stability. It is clear that their elastic coefficients meet the mechanical stability conditions (see Table S2 of SI), indicating that they are at least metastable novel ferroelectric photovoltaic nitrides. To check their thermodynamic stability, the chemical potential phase diagrams were further calculated. Here ternary nitrides are compared with binary nitrides mainly in respect to their formation enthalpy. The calculated chemical potential phase diagrams are provided in Supporting Information (SI) (see Figure S2). It reveals that most of the predicted ternary ferroelectric nitrides here are difficult to be prepared under conventional conditions to achieve thermodynamic stability. This is similar to the preparation of many of the ternary ferroelectric oxides, which may require extreme conditions such as high temperatures and high pressures [33–36]. Ca_2SbN_3 and Mg_2MnN_3 not only have stable chemical potential regions satisfying the thermodynamic stability, but also satisfies the kinetic stability conditions from the phonon and elastic coefficients analysis. The other systems, with kinetic stability but thermal instability, are still metastable, and could be prepared under certain conditions, e.g, with restriction of substrates, etc.

4. Evaluation of ferroelectric photovoltaic performance

The ferroelectric properties and photoelectric conversion efficiencies were calculated to evaluate the ferroelectric photovoltaic performance of the Materials Project and predicted ternary nitrides. Most ferroelectric materials have a relatively large band gap and capture little visible light. The band gap is crucial in determining whether a material can effectively absorb energy from specific wavelengths of sunlight. Ideal photovoltaic materials should possess a band gap width that matches the solar spectrum, typically ranging from 1.1 to 1.7 eV. The excellent ferroelectric photovoltaic materials should have high spontaneous ferroelectric polarization strength, narrow band gap and strong visible light absorption. The ferroelectric spontaneous polarization is calculated using the Born effective charges (BEC) calculation method, and the BEC is obtained using density functional perturbation theory [37]. The centrosymmetric phase of the $Cmc2_1$ structure (X_2YN_3) is chosen as Cmcm, while the centrosymmetric phase of the $Pna2_1$ structure (XYN_2) is Pnma. The calculation of the spontaneous ferroelectric polarization P follows the formula $P = \frac{e}{V}\sum_{j_\beta} Z^*_{j\alpha\beta}\Delta u_j\beta$. Here, Z* is the Born effective charges tensor, and Δu is the relative displacement between the polar and centrosymmetric structures. e and V represent the elementary charge and primitive volume, respectively. As shown in Fig. 3, the energies of the $Cmc2_1$ structure (X_2YN_3) and the $Pna2_1$ structure (XYN_2) show an ideal dual-potential well curve with the change of atomic position, which satisfies the ferroelectric-paraelectric transition reverse. The calculated energy barriers between the ferroelectric and paraelectric phases are listed in Table 2. The energies of polar and centrosymmetric structures are very close to each other for $MgHfN_2$, $MgTiN_2$ and $MgZrN_2$ and their energy barriers are rather tiny, unfavorable to the ferroelectric polarization. The ferroelectric and paraelectric energy barriers of classical ferroelectric oxides $PbTiO_3$ and $BiFeO_3$ are 0.20 eV/f.u [38] and 0.43 eV/f.u [39], respectively. Generally, a larger energy barrier may correspond to a high ferroelectric phase transition

IIA	IIB
Zn	Mg
	Ca
	Sr
	Ba

$Pna2_1$ (XYN_2)			
IVA	IVB	VB	VIB
Ge	Ti	V	Cr
Sn	Zr	Nb	Mo
	Hf	Ta	W

IIA	IIB
Zn	Mg
	Ca
	Sr
	Ba

$Cmc2_1$(X_2YN_3)			
VA	IVB	VB	VIB
Sb	V	Cr	Mn
Bi	Nb	Mo	Tc
	Ta	W	Re

Fig. 2. The combinations of $Cmc2_1$ structures (X_2YN_3) and $Pna2_1$ structures (XYN_2) for prediction of tenary nitrides.

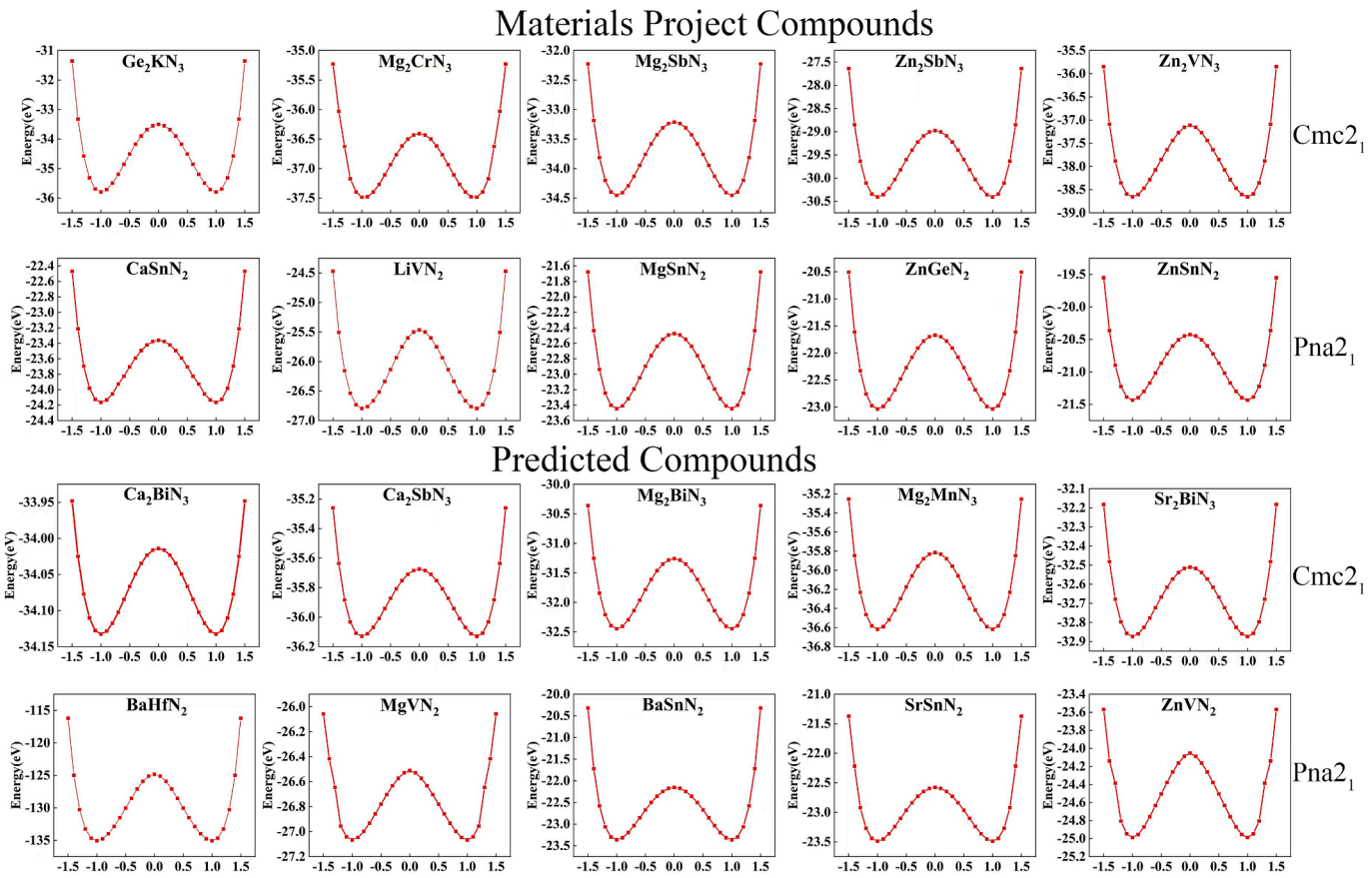

Fig. 3. The calculated energy of atomic movement between ferroelectric and paraelectric phases.

Table 2
The energy barriers per unit cell between the ferroelectric and paraelectric phases for the Materials Project and predicted compounds.

Materials Project Compounds			
$Cmc2_1$		$Pna2_1$	
Compound	Energy (eV)	Compound	Energy (eV)
Mg_2SbN_3	1.24	$CaSnN_2$	0.80
Zn_2VN_3	1.54	$LiVN_2$	1.33
Mg_2CrN_3	1.08	$MgSnN_2$	0.97
$K_2Ge_4N_6$	2.29	$ZnGeN_2$	1.36
Zn_2SbN_3	1.43	$ZnSnN_2$	1.01
Predicted Compounds			
$Cmc2_1$		$Pna2_1$	
Compound	Energy (eV)	Compound	Energy (eV)
Ca_2BiN_3	0.12	$BaSnN_2$	1.21
Ca_2SbN_3	0.46	$BaTiN_2$	0.12
Mg_2BiN_3	1.19	$MgHfN_2$	–
Mg_2MnN_3	0.74	$MgTiN_2$	–
Sr_2BiN_3	0.36	$MgVN_2$	0.56
		$MgZrN_2$	–
		$SrSnN_2$	0.91
		$ZnVN_2$	0.94

temperature.

The photovoltaic conversion efficiency was adopted from the spectroscopic limited maximum efficiency (SLME) approach proposed by Yu and Zunger [40]. The SLME approach considers the effects of band gap, thickness, carrier recombination, and absorption coefficient on the photovoltaic conversion efficiency and is widely used to evaluate the photovoltaic performance of semiconductor materials. The calculated optical absorption coefficients are shown in Fig. 4. Most ferroelectric ternary nitrides in Fig. 4 exhibit strong absorption characteristics in the visible light range, with absorption coefficients reaching up to 10^5 cm^{-1}. The bulk photovoltaic effect and shift current model [41] will be further explored in future studies to investigate the ferroelectric photovoltaic properties. Classic ferroelectric photovoltaic materials $BiFeO_3$ displays an anomalously large photovoltage attributed to the domain wall effect [5]. In our computational study of ferroelectric ternary nitrides, we operated under the assumption that these materials behaved as single-domain ferroelectric compounds, overlooking the influence of domain walls. Further investigations are warranted to explore the potential implications of domain wall effects on the photovoltaic properties of these materials. The band gap values, ferroelectric polarization strength, and maximum photovoltaic conversion efficiency for the $Cmc2_1$ structure (X_2YN_3) and the $Pna2_1$ structure (XYN_2) are shown in Fig. 5. The circular represents the structure in the Materials Project, while the pentagonal represents the predicted structure in Fig. 5. The maximum photovoltaic conversion efficiency mainly considers the ideal solar cell efficiency for the material at 0.5 μm thickness. As shown in Fig. 5, two approaches may be considered to achieve high ferroelectric polarization strength and high photoelectric conversion efficiency in ternary nitrides, namely the participation of Bi element or 3d transition metal ions with low electron configuration.

X_2BiN_3 (X = Mg, Ca, and Sr) has an ideal band gap (about 1.5 eV) and high SLME photoelectric conversion efficiency. At the same time, X_2BiN_3 (X = Mg, Ca, and Sr) can also maintain an excellent ferroelectric property with large ferroelectric polarization strength and high energy barriers between the ferroelectric and paraelectric. Bi-based oxides are widely applied in visible-light photocatalytic materials because of the special Bi-6s and Bi-6p energy levels, reducing the band gap [42]. These calculated ferroelectric nitrides as strong candidates for high-efficiency ferroelectric photovoltaics have a more desirable band gap and high ferroelectric polarization strength than the earlier ferroelectric oxides or

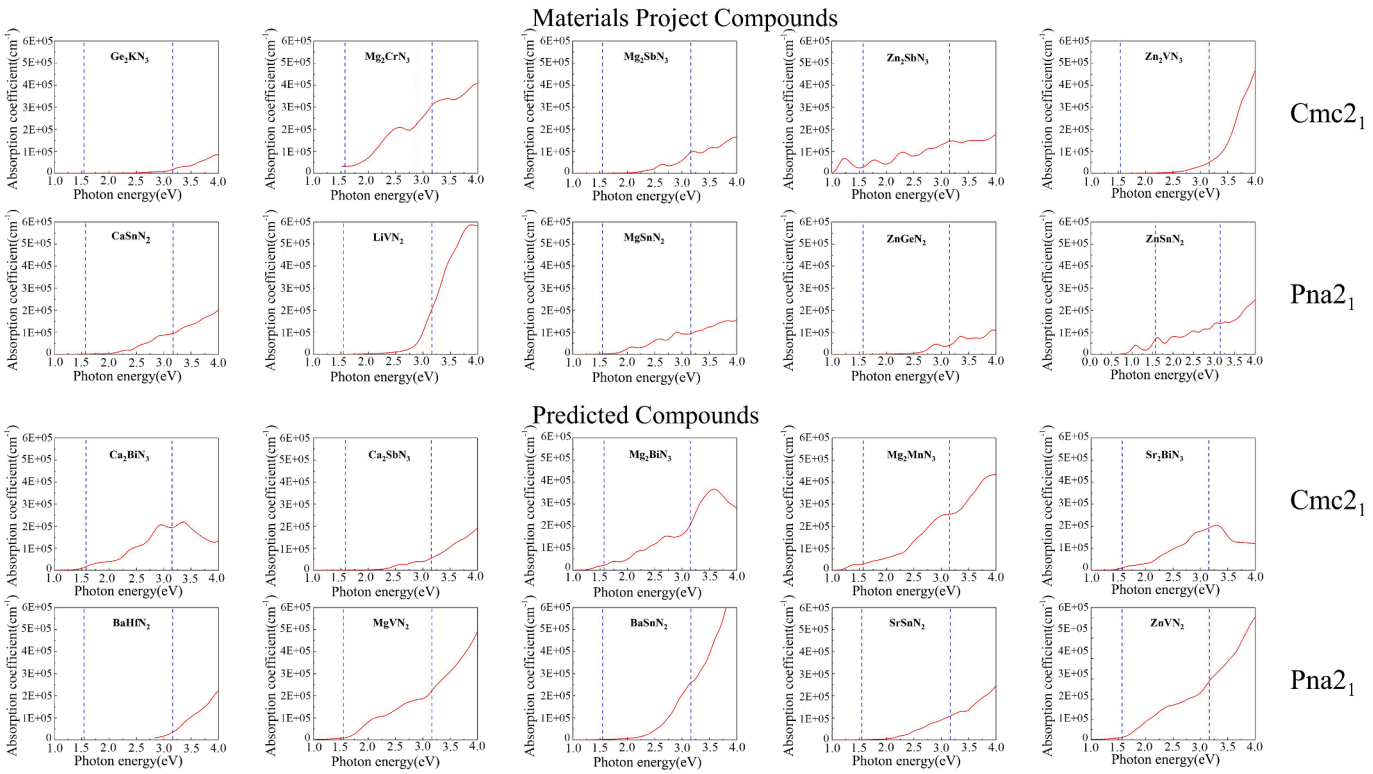

Fig. 4. The calculated optical absorption coefficients with the area between the two dashed lines representing the absorption range of visible light.

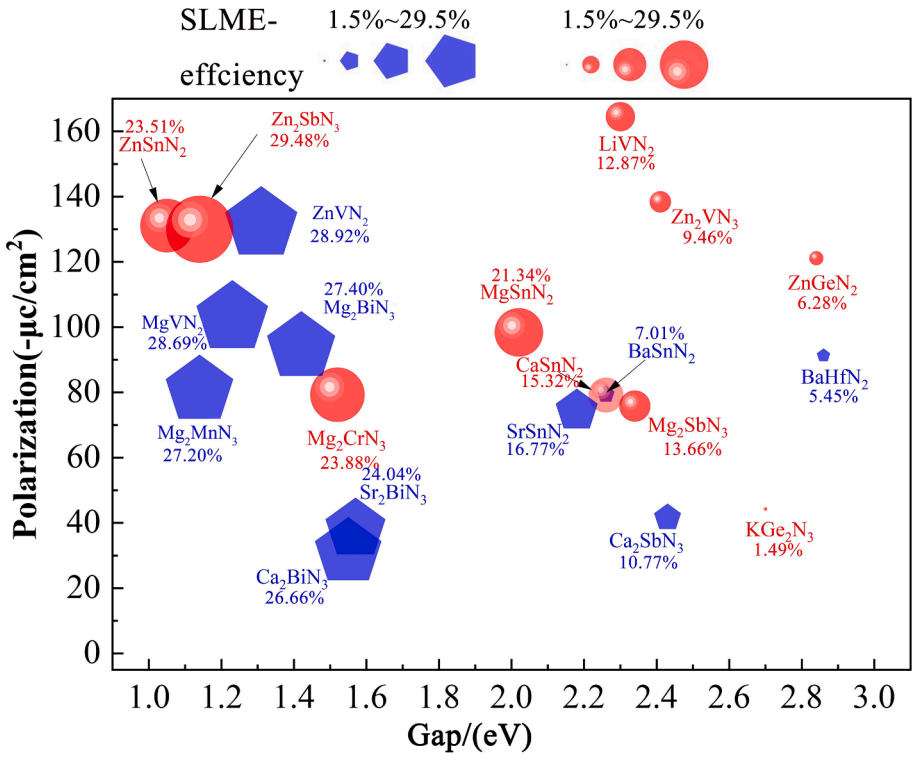

Fig. 5. The band gap, ferroelectric polarization strength, and SLME efficiency of Materials Project (red ball) and predicted (blue pentagon) compounds. The size of the balls and pentagons indicates SLME efficiency. (For interpretation of the references to colour in this figure legend, the reader is referred to the web version of this article.)

sulfides such as $BiFeO_3$[43], Bi_2FeCrO_6 [44], $XBiO_3$ (X = Ca,Mg,Cd and Zn) [45], $TbMnO_3$ [46], $CuGaO_2$ [47], $ZnSnS_3$ [48] and $MgSnS_3$ [49]. The calculated density of states of X_2BiN_3 (X = Mg, Ca, and Sr) are shown in Fig. 6. N-2*p* energy level mainly occupies the valence band, while the conduction band mainly comprises the antibonding states composed of Bi-6*s* and N-2*p* energy levels. The antibonding state

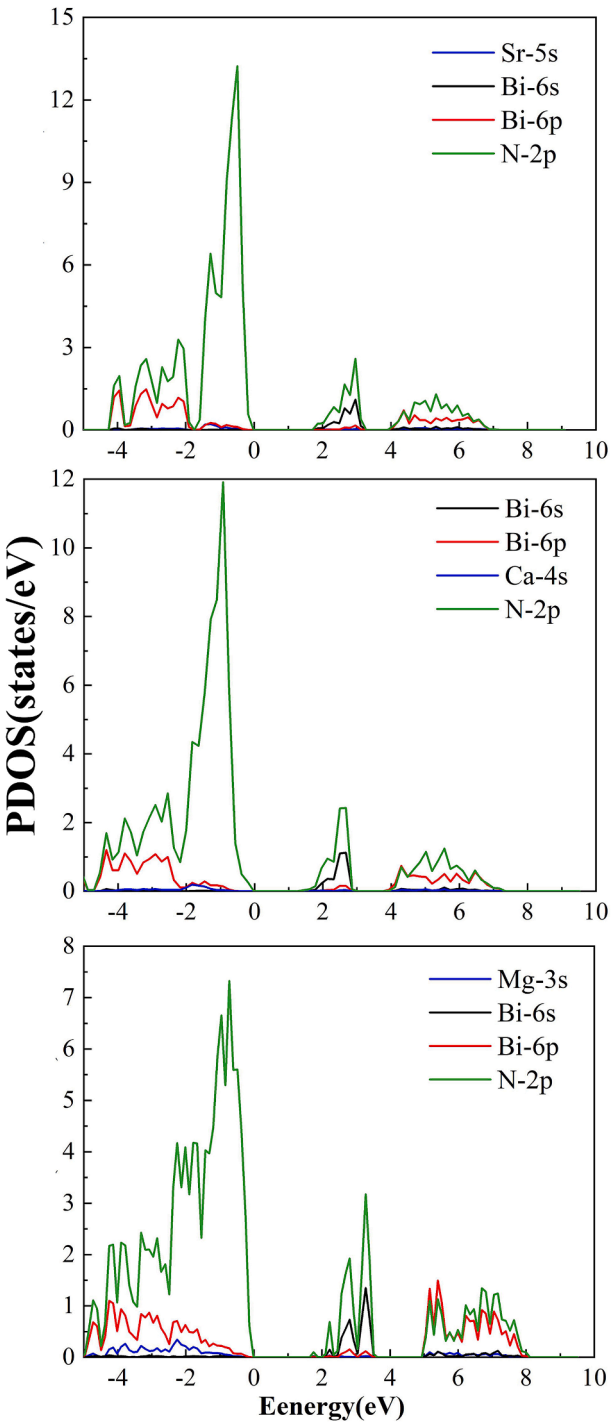

Fig. 6. The calculated density of states of X_2BiN_3 (X = Mg, Ca, and Sr).

composed of Bi-6*s* and N-2*p* energy levels is beneficial to reducing the material to the visible light range. The electronic transition of the *s* and *p* levels could also be promoted for the bulk ferroelectric photovoltaic effect according to the shift current model [50].

Another class of potentially stable ferroelectric photovoltaic ternary metal nitrides is Mg_2CrN_3, Mg_2MnN_3, $MgVN_2$, and $ZnVN_2$ compounds with 3*d* transition metal of low electron configuration. They have relatively suitable band gaps and high SLME photoelectric conversion efficiencies, as well as large ferroelectric polarization strengths. Mg_2CrN_3, Mg_2MnN_3, $MgVN_2$, and $ZnVN_2$ have ferroelectric and magnetic properties and constitute multiferroic materials with rich physical properties [51]. The band gaps of Mg_2XN_3 (X = V, Cr, Mn, Fe, Co, and Ni) and $ZnXN_2$ (X = V, Cr, Mn, Fe, Co, and Ni) were further calculated to evaluate the ferroelectric photovoltaic effect. Following the general rules, it is clear that the band gaps in Table 3 decreases with the increase of the atomic number. The 3*d* transition metal with a low electron configuration could benefit ferroelectric photovoltaic performance. The calculated density of states of Mg_2CrN_3, Mg_2MnN_3, $MgVN_2$, and $ZnVN_2$ in Fig. 7 show that the 3*d* transition metal with low electron configuration (V, Cr, Mn) can form bonding and antibonding states with the N-2*p* energy level near the valence and conduction bands. The interactions between the 3*d* energy level with low electron configuration and the N-2*p* energy level play an essential role in the high efficiency of ferroelectric photovoltaic nitride.

The high absorption coefficient and the strong ferroelectric polarization strength are favorable for the photogenerated carriers. The transport properties of the carriers after generation are also an important consideration for photovoltaic devices. Materials with high carrier mobility are an important reference for achieving high photovoltaic efficiency. The carrier mobilities of $BiFeO_3$, Bi_2FeCrO_6, X_2BiN_3 (X = Mg, Ca, and Sr), Mg_2CrN_3, Mg_2MnN_3, $MgVN_2$, and $ZnVN_2$ are calculated by the AMSET code with considering the ionized impurity (IMP) scattering, the acoustic deformation potential (ADP) scattering, the piezoelectric scattering (PE) and the polar optical phonon (POP) scattering [52]. The impurity charge and static dielectric constant are applied to the IMP scattering. The deformation potential and elastic constant are considered in the ADP scattering. The piezoelectric coefficient and static dielectric is used for the PE scattering. The POP scattering is related to the polar optical phonon frequency, static dielectric constant and high frequency dielectric. The calculated deformation potential, piezoelectric coefficient, static dielectric constant and high frequency dielectric as the input parameter of AMSET code are listed in Supporting Information (see Table S4, Table S5 and Table S6). The calculated carrier mobilities at 300 K are shown in Fig. 8 and Table 4. The calculations reveal that the carrier mobilities of ferroelectric ternary nitrides with polar structure in Fig. 8 are mainly dominated by the POP scattering, which is similar to binary polar structure GaN [52]. The electron mobilities of X_2BiN_3 (X = Mg, Ca, and Sr) and Mg_2MnN_3 are larger than the classic ferroelectric photovoltaic oxide $BiFeO_3$,Bi_2FeCrO_6 and halide perovskites $MAPbI_3$ (67 $cm^2\ V^{-1}\ s^{-1}$) [53] due to the the small static dielectric constant, large high frequency dielectric and small carrier effective mass.

5. Conclusion

In summary, we have carried out a high-throughput search for ternary nitrides with ferroelectric photovoltaic properties. There are 27 ternary nitrides as candidates based on the conditions of convex hull energy, polar space group, and band gap. The new stable ternary nitride ferroelectric photovoltaic materials with $Cmc2_1$ structure (X_2YN_3) and $Pna2_1$ structure (XYN_2) were predicted by screening results and paired combination. We demonstrate that the participation of Bi element or early 3*d* transition metal ions can achieve ferroelectric photovoltaic nitrides with high ferroelectric polarization and high photoelectric conversion efficiency. Bi-6 *s* and N-2*p* interactions in X_2BiN_3 (X = Mg, Ca, and Sr) are beneficial to the ferroelectric photovoltaic performance. The interaction of 3*d* level and N-2*p* level of low electron configurations of Mg_2CrN_3, Mg_2MnN_3, $MgVN_2$, and $ZnVN_2$ plays a critical role in

Table 3
The calculated band gap of Mg_2XN_3 (X = V, Cr, Mn, Fe, Co and Ni) and $ZnXN_2$ (X = V, Cr, Mn, Fe, Co and Ni). FM stands for ferromagnetic coupling, while AFM stands for antiferromagnetic coupling. The unit gives in eV.

	V	Cr	Mn	Fe	Co	Ni
Mg_2XN_3	3.0 (AFM)	1.7 (FM)	1.1 (FM)	1.0 (AFM)	0 (FM)	0 (AFM)
$ZnXN_2$	1.3 (FM)	0.46 (FM)	0 (FM)	0 (FM)	0 (AFM)	0 (AFM)

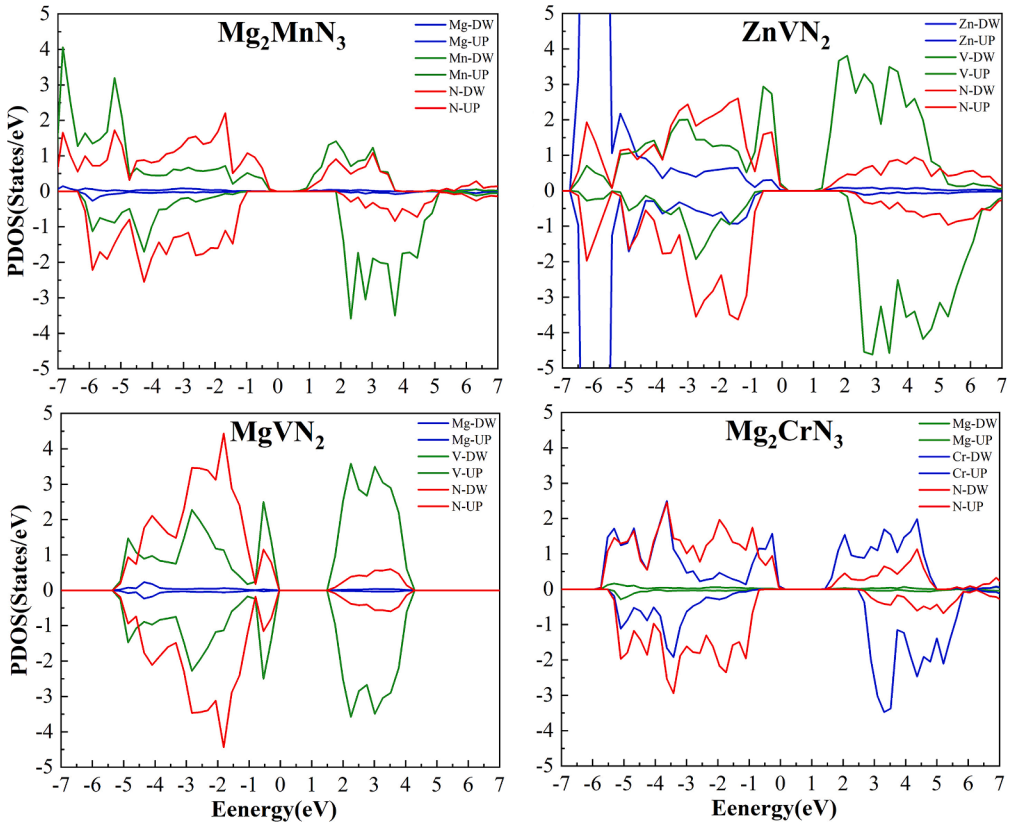

Fig. 7. The calculated density of states of Mg_2CrN_3, Mg_2MnN_3, $MgVN_2$, and $ZnVN_2$.

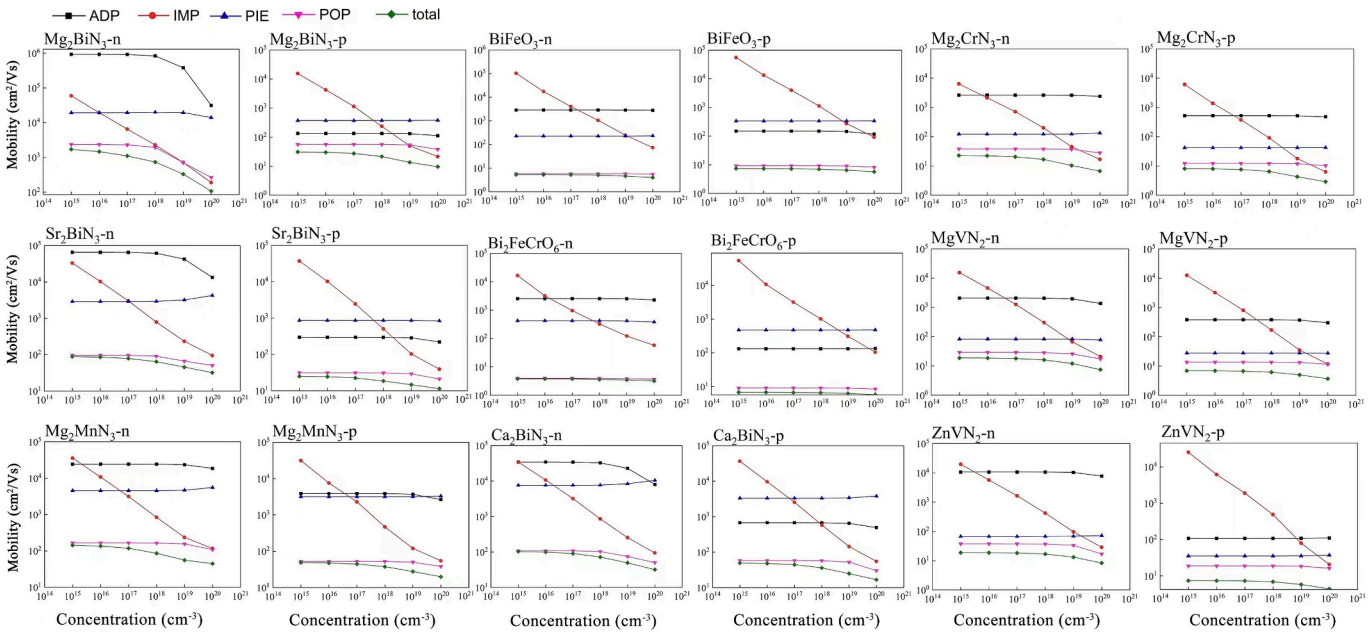

Fig. 8. The calculated carrier mobilities with ionized impurity scattering, the acoustic deformation potential scattering, the piezoelectric scattering and the polar optical phonon scattering.

achieving high-efficiency ferroelectric photovoltaic performance. Their carrier mobility is mainly affected by polar optical phonon scattering, while the high carrier mobility combined with the strong ferroelectric polarization electric field is very favorable for carrier transport. These studies can expand the application of nitrides in the field of ferroelectric photovoltaics.

6. Computational methods

The first-principles calculations were mainly performed by the projector augmented-wave (PAW) method and the Perdew–Burke–Ernzerhof (PBE) or the Heyd–Scuseria–Ernzerhof (HSE06) hybrid functional, as implemented in the Vienna Ab initio Simulation

Table 4
The calculated carrier mobilities μ_e (electron) and μ_h (hole) ($cm^2V^{-1}s^{-1}$) at 300 K with different concentration (cm^{-3}).

		10^{15}	10^{16}	10^{17}	10^{18}	10^{19}	10^{20}
$BiFeO_3$	μ_e	5.3	5.3	5.2	5.1	4.6	4.0
	μ_h	7.4	7.3	7.2	7.0	6.5	5.7
Bi_2FeCrO_6	μ_e	3.8	3.8	3.8	3.6	3.5	3.2
	μ_h	6.8	6.8	6.7	6.6	6.3	5.8
Ca_2BiN_3	μ_e	103.2	99.6	90.6	72.1	49.6	31.8
	μ_h	49.4	48.1	44.4	36.1	24.9	16.7
Mg_2BiN_3	μ_e	1707.6	1465.9	1104.6	737.8	331.1	106.8
	μ_h	30.9	30	27.5	21.5	13.6	9.6
Sr_2BiN_3	μ_e	88.2	85.5	78.6	63.9	45.4	31.9
	μ_h	25	24.4	22.5	18.6	14.7	11.4
Mg_2MnN_3	μ_e	142.9	135.6	118.2	86.1	55.7	44.6
	μ_h	49	47.7	44.4	37.5	27.7	19.8
Mg_2CrN_3	μ_e	22.9	22.2	20.6	16.8	10.4	6.7
	μ_h	8.1	8	7.6	6.5	4.3	2.9
$MgVN_2$	μ_e	18.8	18.6	18	16.2	12.1	7.5
	μ_h	6.9	6.9	6.7	6.2	5	3.7
$ZnVN_2$	μ_e	18.9	18.8	18.4	17	13.3	8.4
	μ_h	7.4	7.4	7.3	6.9	5.8	4.4

Package (VASP) [54,55]. The high-throughput band gap calculations are obtained using the norm-conserving pseudopotential (NCPP-SG15) and HSE06 hybrid functional, as implemented in the PWMAT software [56–58]. The SCAN (Strongly constrained and appropriately normed) functional is carried out to calculate the formation enthalpy in the VASP, which is more accurate in calculating the total energy [59]. Hubbard U correction (U_{eff} = 4 eV) was applied to the 3*d* transition metals for the structure, and lattice dynamic stability calculations [60]. In typical scenarios, determining the precise Hubbard U values for 3d transition metals necessitates the use of the linear response approach [61]. Considering the complexity of our computational setup, we chose a representative value of U_{eff} = 4 eV, providing a reasonable approximation for the interactions of transition metals. Additionally, our analysis of band gaps and electronic structures was based on calculations performed using the HSE06 functional. Renowned for its high precision, HSE06 has proven to be highly effective in computational studies.The HSE06 hybrid functional was employed for evaluating the band gaps, electron density of states analysis and optical absorption properties, while the absorption coefficients are acquired from the complex frequency-dependent dielectric matrix by the random phase approximation (RPA) scheme. The berry phase method [62,63]was employed to compute the ferroelectric polarization strength of materials, encompassing X_2BiN_3 (where X = Mg, Ca, and Sr), Mg_2CrN_3, Mg_2MnN_3, $MgVN_2$, and $ZnVN_2$. Detailed computational procedures and results are elaborated upon in the Supporting Information (SI) (see Figure S3 and Table S7). The ferroelectric polarization strength calculated using berry phase method for these compounds demonstrates a close alignment with the results derived from Born effective charge calculations.

CRediT authorship contribution statement

Guo-Xia Lai: Writing – original draft. **Jin-Long Yang:** Formal analysis. **Hua-Kai Xu:** Software. **Wen-Ce Li:** Investigation. **Kun-Ren Su:** Validation. **Xiang-Fu Xu:** Data curation. **Wei-Ling Zhu:** Formal analysis. **Xing-Yuan Chen:** Writing – review & editing. **Xiao-Bao Yang:** Supervision. **Yu-Jun Zhao:** Supervision.

Declaration of competing interest

The authors declare that they have no known competing financial interests or personal relationships that could have appeared to influence the work reported in this paper.

Data availability

Data will be made available on request.

Acknowledgement:

This work was supported by National Natural Science Foundation of China (Grant No. 12074441), the Natural Science Foundation of Guangdong Province, China (Grant No. 2021S055), Guangdong Provincial Key Areas Special Project for Regular Higher Education Institutions (Grant No. 2023ZDZX3014), Guangdong University Student Climbing Project (Grant No. pdjh2023b0357) .

Appendix A. Supplementary material

Supplementary data to this article can be found online at https://doi.org/10.1016/j.commatsci.2024.112962.

References

[1] P. Lopez-Varo, L. Bertoluzzi, J. Bisquert, et al., Physical aspects of ferroelectric semiconductors for photovoltaic solar energy conversion[J], Phys. Rep 653 (2016) 1–40.
[2] K. Meng, W. Li, X.G. Tang, et al., A review of a good binary ferroelectric ceramic: BaTiO3–BiFeO3[J], ACS Appl. Electron. Mater 4 (5) (2021) 2109–2145.
[3] K.T. Butler, J.M. Frost, A. Walsh, Ferroelectric materials for solar energy conversion: photoferroics revisited [J], Energy Environ. Sci 8 (3) (2015) 838–848.
[4] J. Wang, J.B. Neaton, H. Zheng, et al., Epitaxial BiFeO3 multiferroic thin film heterostructures[J], Science 299 (5613) (2003) 1719–1722.
[5] S.Y. Yang, J. Seidel, S.J. Byrnes, et al., Above-bandgap voltages from ferroelectric photovoltaic devices[J], Nat. Nanotechnol 5 (2) (2010) 143–147.
[6] Y. Bai, H. Jantunen, J. Juuti, Ferroelectric oxides for solar energy conversion, multi-source energy harvesting/sensing, and opto-ferroelectric applications[J], Chem Sus Chem 12 (12) (2019) 2540–2549.
[7] S. Shahrokhi, W. Gao, Y. Wang, et al., Emergence of ferroelectricity in halide perovskites[J], Small Methods 4 (8) (2020) 2000149.
[8] W. Zhang, M. Hong, J. Luo, Halide double perovskite ferroelectrics[J], Angew. Chem 132 (24) (2020) 9391–9394.
[9] P. Höhn, R. Niewa, Nitrides of non-main group elements [J], Part, CRC Handb. Solid Sta Electrochem, 2017, p. 1.
[10] A. Zakutayev, S.R. Bauers, S. Lany, Experimental synthesis of theoretically predicted multivalent Ternary nitride Materials[J], Chem. Mater 34 (4) (2022) 1418–1438.
[11] P.K. Todd, M.J. Fallon, J.R. Neilson, et al., Two-step solid-state synthesis of ternary nitride materials[J], ACS Mater. Lett 3 (12) (2021) 1677–1683.
[12] A.L. Greenaway, C.L. Melamed, M.B. Tellekamp, et al., Ternary nitride materials: fundamentals and emerging device applications[J], Annu. Rev. Mater. Res. 51 (2021) 591–618.
[13] R. Sarmiento-Perez, T.F.T. Cerqueira, S. Körbel, et al., Prediction of stable nitride perovskites[J], Chem. Mater 27 (17) (2015) 5957–5963.
[14] A. Zakutayev, Design of nitride semiconductors for solar energy conversion[J], J. Mater. Chem. A 4 (18) (2016) 6742–6754.
[15] W. Sun, C.J. Bartel, E. Arca, et al., A map of the inorganic ternary metal nitrides[J], Nat. Mater 18 (7) (2019) 732–739.
[16] Y. Hinuma, T. Hatakeyama, Y. Kumagai, et al., Discovery of earth-abundant nitride semiconductors by computational screening and high-pressure synthesis[J], Nat. Commun 7 (1) (2016) 1–10.
[17] K.N. Heinselman, S. Lany, J.D. Perkins, et al., Thin film synthesis of semiconductors in the Mg–Sb–N materials system[J], Chem. Mater 31 (21) (2019) 8717–8724.
[18] Y.W. Fang, C.A.J. Fisher, A. Kuwabara, et al., Lattice dynamics and ferroelectric properties of the nitride perovskite LaWN 3[J], Phys. Rev. B 95 (1) (2017) 014111.
[19] C. Gui, S. Dong, Pressure-induced ferroelectric phase of LaMoN3[J], Phys. Rev. B 102 (18) (2020) 180103.
[20] M. Hu, X. Yang, T. Su, et al., Ferroic properties and piezoelectric response of Mg2XN3 (X= V, cr) [J], Appl. Phys. Lett 118 (12) (2021) 122903.
[21] K.R. Talley, C.L. Perkins, D.R. Diercks, et al., Synthesis of LaWN3 nitride perovskite with polar symmetry[J], Science 374 (6574) (2021) 1488–1491.
[22] V.A. Ha, H. Lee, F. Giustino, CeTaN3 and CeNbN3: prospective nitride perovskites with optimal photovoltaic band Gaps[J], Chem. Mater 34 (5) (2022) 2107–2122.
[23] S. Zhuk, A.A. Kistanov, S.C. Boehme, et al., Synthesis and Characterization of the Ternary nitride semiconductor Zn2VN3: theoretical prediction, combinatorial screening, and epitaxial Stabilization[J], Chem. Mater 33 (23) (2021) 9306–9316.
[24] P. Xue, D. Chu, C. Xie, et al., Design of new Ternary Nitrides for photovoltaic applications via high-throughput Calculations[J], J. Phys. Chem. C 126 (40) (2022) 17398–17405.
[25] X.Y. Chen, J.L. Yang, L.F. Chen, et al., Theoretical study on the ferroelectric nitrides with super-wurtzite structure for solar energy conversion applications[J], Phys. Chem. Chem. Phys 24 (48) (2022) 29570–29578.

[26] J.J. de Pablo, N.E. Jackson, M.A. Webb, et al., New frontiers for the materials genome initiative[J], Npj Comput. Mater 5 (1) (2019) 1–23.
[27] A. Jain, S.P. Ong, G. Hautier, et al., The materials project: a materials genome approach to accelerating materials innovation, [J] APL Mater (2013,1 (1):) 011002.
[28] S.P. Ong, W.D. Richards, A. Jain, et al., Python materials genomics (pymatgen): a robust, open-source python library for materials analysis[J], Comput. Mater. Sci 68 (2013) 314–319.
[29] J.P. Perdew, K. Burke, M. Ernzerhof, [J] Phys, Rev. Lett. 77 (1996) 3865–3868.
[30] J. Hafner, Ab-initio simulations of materials using VASP: density-functional theory and beyond[j], J. Comput. Chem 29 (13) (2008) 2044–2078.
[31] B.G. Janesko, T.M. Henderson, G.E. Scuseria, Screened hybrid density functionals for solid-state chemistry and physics[J], Phys. Chem. Chem. Phys 11 (3) (2009) 443–454.
[32] M. Jain, J.R. Chelikowsky, S.G. Louie, Reliability of hybrid functionals in predicting band gaps[J], Phys. Rev. Lett 107 (21) (2011) 216806.
[33] T. Varga, A. Kumar, E. Vlahos, et al., Coexistence of weak ferromagnetism and ferroelectricity in the high pressure LiNbO3-type phase of FeTiO3[J].Phys, Rev. Lett. 103 (4) (2009) 047601.
[34] Y. Inaguma, A. Aimi, Y. Shirako, et al., High-pressure synthesis, crystal structure, and phase stability relations of a LiNbO3-type polar titanate ZnTiO3 and its reinforced polarity by the second-order jahn-teller effect[J], J. Am. Chem. Soc 136 (7) (2014) 2748–2756.
[35] W. Sun, S.T. Dacek, S.P. Ong, et al., The thermodynamic scale of inorganic crystalline metastability[J], Sci. Adv 2 (11) (2016) e1600225.
[36] Y. Han, M. Wu, C. Gui, et al., Data-driven computational prediction and experimental realization of exotic perovskite-related polar magnets[J], Npj Quantum Materials 5 (1) (2020) 1–9.
[37] M. Gajdoš, K. Hummer, G. Kresse, et al., Linear optical properties in the projector-augmented wave methodology[J], Phys. Rev. B 73 (4) (2006) 045112.
[38] C. Ederer, N.A. Spaldin, Effect of epitaxial strain on the spontaneous polarization of thin film ferroelectrics[J], Phys. Rev. Lett 95 (25) (2005) 257601.
[39] J.B. Neaton, C. Ederer, U.V. Waghmare, et al., First-principles study of spontaneous polarization in multiferroic BiFeO3[J], Phys. Rev. B 71 (1) (2005) 014113.
[40] L. Yu, A. Zunger, Identification of potential photovoltaic absorbers based on first-principles spectroscopic screening of materials[J], Phys. Rev. Lett 108 (6) (2012) 068701.
[41] S.M. Young, A.M. Rappe, First principles calculation of the shift current photovoltaic effect in ferroelectrics[J], Phys. Rev. Lett 109 (11) (2012) 116601.
[42] P. Chen, H. Liu, W. Cui, et al., Bi-based photocatalysts for light-driven environmental and energy applications: structural tuning, reaction mechanisms, and challenges[J], Eco Mat 2 (3) (2020) e12047.
[43] J.F. Ihlefeld, N.J. Podraza, Z.K. Liu, et al., Optical band gap of BiFeO3 grown by molecular-beam epitaxy[J], Appl. Phys. Lett 92 (14) (2008) 142908.
[44] S. Li, B. AlOtaibi, W. Huang, et al., Epitaxial Bi2FeCrO6 multiferroic thin film as a new visible light absorbing photocathode material[J], Small 11 (32) (2015) 4018–4026.
[45] J. He, C. Franchini, J.M. Rondinelli, Ferroelectric oxides with strong visible-light absorption from Charge ordering. [J], Chem. Mater. 29 (2017) 2445–2451.
[46] X. Huang, T.R. Paudel, S. Dong, E.Y. Tsymbal, Hexagonal Rare-Earth manganites as promising photovoltaics and light Polar- izers. [J], Phys. Rev. b: Condens. Matter Mater. Phys. 92 (2015) 125201.
[47] S. Song, D. Kim, H.M. Jang, et al., β-CuGaO2 as a strong candidate material for efficient ferroelectric photovoltaics[J], Chem. Mater 29 (17) (2017) 7596–7603.
[48] B. Kolb, A.M. Kolpak, First-principles design and analysis of an efficient, pb-free ferroelectric photovoltaic absorber derived from ZnSnO3[J], Chem. Mater 27 (17) (2015) 5899–5906.
[49] X.Y. Chen, J.Q. Tan, K.R. Su, et al., First-principles study of R3c-MgSnX3 (X=O, S and se) for photovoltaic and ferroelectric application[J], Phys Lett A 422 (2022) 127774.
[50] L.Z. Tan, F. Zheng, S.M. Young, et al., Shift current bulk photovoltaic effect in polar materials—hybrid and oxide perovskites and beyond [J] npj, Comput. Mater 1 (2016) 12.
[51] W. Eerenstein, N.D. Mathur, J.F. Scott, Multiferroic and magnetoelectric materials [J], Nature 442 (7104) (2006) 759–765.
[52] A.M. Ganose, et al., Efficient calculation of carrier scattering rates from first principles, [J] nat, Commun. 12 (1) (2021) 1–9.
[53] S. Poncé, M. Schlipf, F. Giustino, Origin of low carriermobilities in halide perovskites, [J] ACS Energy Lett., 2019, 4(2),456–463.
[54] A.N.E.S.M. Kozlov, F. Viñes, F. Illas, Electronic-structure-based chemical descriptors:(in) dependence on self-interaction and Hartree-fock exchange[J], Phys. Rev. B 54 (1996) 11169–11186.
[55] G. Kresse, D. Joubert, From ultrasoft pseudopotentials to the projector augmented-wave method[J], Phys. Rev. B 59 (3) (1999) 1758–1775.
[56] W. Jia, J. Fu, Z. Cao, et al., Fast plane wave density functional theory molecular dynamics calculations on multi-GPU machines[J], J. Comput. Phys. 251 (2013) 102–115.
[57] W. Jia, Z. Cao, L. Wang, et al., The analysis of a plane wave pseudopotential density functional theory code on a GPU machine[J], Comput. Phys. Commun 184 (1) (2013) 9–18.
[58] D.R. Hamann, Optimized norm-conserving vanderbilt pseudopotentials[J], Phys. Rev. B 88 (8) (2013) 085117.
[59] J. Sun, A. Ruzsinszky, J.P. Perdew, Strongly constrained and appropriately normed semilocal density functional[J], Phys. Rev. Lett 115 (3) (2015) 036402.
[60] V.I. Anisimov, J. Zaanen, O.K. Andersen, Band theory and Mott insulators: Hubbard U instead of stoner I[J], Phys. Rev. B 44 (3) (1991) 943.
[61] M. Cococcioni, S. De Gironcoli, Linear response approach to the calculation of the effective interaction parameters in the LDA+ U method[J], Phys. Rev. B 71 (3) (2005) 035105.
[62] R. Resta, Macroscopic polarization in crystalline dielectrics: the geometric phase approach[J], Rev. Mod. Phys. 66 (3) (1994) 899.
[63] N.A. Spaldin, A beginner's guide to the modern theory of polarization[J], J Solid State Chem. 195 (2012) 2.